The Meteoritical Society

Meteoritics & Planetary Science 58, Nr 4, 529–545 (2023)
doi: 10.1111/maps.13970

Impacts on the CV parent body: A coordinated, multiscale fabric analysis of the Allende meteorite

L. V. FORMAN[1,2]*, L. DALY[2,3,4], P. A. BLAND[1], G. K. BENEDIX[1,2,5], and C. CORRIGAN[6]

[1]Space Science & Technology Centre, School of Earth & Planetary Sciences, Curtin University, Bentley, Western Australia, Australia
[2]Department of Earth & Planetary Sciences, Western Australian Museum, Perth, Western Australia, Australia
[3]School of Geographical & Earth Sciences, University of Glasgow, Glasgow, UK
[4]Australian Centre for Microscopy and Microanalysis, University of Sydney, Sydney, New South Wales, Australia
[5]Planetary Science Institute, Tucson, Arizona, USA
[6]Department of Mineral Science, National Museum of Natural History (NMNH), Washington, DC, USA
*Corresponding author.
L. V. Forman, Space Science & Technology Centre, School of Earth & Planetary Sciences, GPO Box U1987, Bentley, WA 6845, Australia.
E-mail: lucy.forman@curtin.edu.au

(Received 06 October 2022; revision accepted 02 March 2023)

Abstract–Evidence of impact-induced compaction in the carbonaceous chondrites, specifically CMs and CVs, has been widely investigated utilizing microscopy techniques and impact experiments. Here, we use high-resolution photography and large area and high-resolution electron backscattered diffraction (EBSD) mapping analyses in tandem, to explore the effects of impact-induced compaction at both the meso- and micro-scales in the Allende CV3.6 carbonaceous chondrite. Macro-scale photography images of a ~25 cm slab of Allende captured meso-scale features including calcium-aluminum inclusions (CAIs) and chondrules. CAIs have a long-axis shape-preferred orientation (SPO). Examination of such meso-scale features in thin section revealed the same trend. Matrix grains from this section display a large amount of heterogeneity in petrofabric orientation; microscale, high-resolution, large area EBSD mapping of ~300,000 olivine matrix grains; high-resolution large area EBSD map across an elongate CAI; and a series of high-resolution EBSD maps around two chondrules and around the CAI revealed crystallographic preferred orientations (CPOs) in different directions. Finally, internal grains of the CAI were found to demonstrate a weak lineation CPO, the first crystallographic detection of possible CAI "flow." All results are consistent with multiple, gentle impacts on the Allende parent body causing hemispheric compaction. The larger, more resistant components are likely to have been compressed and oriented by earlier impacts, and the matrix region petrofabrics and CAI "flow" likely occurred during subsequent impacts. Meteoritic components respond differently to impact events, and consequently, it is likely that different components would retain evidence of different impact events and angles.

INTRODUCTION

Early planetary bodies formed via accretion of tiny dust particles to create highly porous, "fluffy" bodies (Bland et al., 2011; Blum, 2003; Blum & Schräpler, 2004; Ormel et al., 2008). Such bodies had much higher porosities (~70% matrix porosity) than are observed in meteorites today (Bland et al., 2011). Post-accretion, many undifferentiated planetary bodies experienced thermal and aqueous alteration, as evidenced by melt textures, mineral replacement at moderate–high temperatures, the presence of hydrated and dehydrated phyllosilicates and sulfates, and carbonate-rich veins in chondritic meteorites (Bland et al., 2009; Grimm & Mcsween, 1989; Keil, 2000; Kimura et al., 2008; McCoy, 2010), which may have acted to reduce or modify the initial porosity of the material. Relatively unaltered, petrologic type 3 (Dodd, 1981; Schmus & Wood, 1967; Sears & Dodd, 1988) and

"unshocked" chondrites (S1-2; Scott et al., 1992; Sharp & DeCarli, 2006; Stöffler et al., 1991) would therefore be expected to display high matrix porosities akin to the early, "fluffy" planetesimals, as such materials have not undergone extensive thermal, aqueous, or typical shock processing that act to reduce their porosity. This, however, is not the case. Estimates of matrix porosity for planetary bodies at the post-accretion and pre-compaction stage are as high as ~70% (Bland et al., 2011, 2014; Davison et al., 2012), yet these porosities are rarely observed in any type 3 carbonaceous chondrites (Corrigan et al., 1997; Macke et al., 2011). Meteorites that have undergone significant aqueous alteration typically show decreasing porosities with increasing degree of alteration (Lindgren et al., 2015), and so the predicted high matrix porosities for early bodies (Bland et al., 2011, 2014; Davison et al., 2012) have not been detected within this population either. The CO3 Ornans is an anomaly; with a bulk porosity of up to ~41% (Macke et al., 2011), it is likely that this meteorite has retained much of its primordial matrix porosity, possibly owing to the high abundance of zero-porosity chondrules present in this meteorite. Nevertheless, planetesimal-wide compaction processes must have occurred on most planetary bodies in the early stages of post-accretion planetary evolution, including those bodies of petrologic type 3 that are considered to have undergone limited to no alteration (Keller et al., 1994; Scott et al., 1992). This compaction process would have acted to lithify the accreted dust particles, and in turn compact the planetary materials to generate porosities at the magnitude observed in meteorites today.

There is, as yet, no consensus in the literature regarding the predominant process by which porosity reduction occurred in these primitive fluffy objects. Small bodies that were unable to generate sufficient gravity to compact their materials are of specific interest in this study, that is, chondritic planetary bodies, as meteorites from such bodies are least likely to have early processing overprinted by alteration. Studies have demonstrated both internal heating (Gail et al., 2015; Henke et al., 2012) and impact (Bland et al., 2011; Davison et al., 2017; Forman et al., 2016, 2017; Muxworthy et al., 2017; Scott et al., 1992) are potential drivers or contributors to compaction at this scale. It is postulated that internal heating-related compaction is driven by hot isostatic pressing, whereby heat sourced from short-lived radionuclides, specifically Al^{26}, drives the process of sintering and slow compaction of the individual planetary components into a larger body (Gail et al., 2015; Henke et al., 2012). Impact-induced compaction is driven by (relatively) low velocity impacts (~1.5 km s^{-1}) during the early stages of planetary body evolution (Bland et al., 2011, 2014). Here, we focus on the Allende CV 3.6 meteorite whose textures have been shown to be dominated by impact-induced compaction (Forman et al., 2016, 2017, 2019; Watt et al., 2006), as such, in this study, we primarily consider the effects of impact-induced compaction.

Allende is a relatively unaltered meteorite (type 3.6; Bonal et al., 2006) and exhibits a low level of shock (S1; Scott et al., 1992). This makes Allende an excellent candidate sample for considering early compaction processes. In addition, many studies have documented the shape elongation of components within CV chondrites at the macro-scale, such as calcium-aluminum inclusions (CAIs) and chondrules (Keller et al., 1994; Nakamura et al., 1992, 1995, 2000; Scott et al., 1992; Tait et al., 2016) or the crystallographic alignments of micro-scale components, such as foliations within matrix (Bland et al., 2011; Forman et al., 2016, 2017, 2019; Muxworthy et al., 2017; Watt et al., 2006), all of which are attributed to compaction. A preferred shape orientation foliation in chondrule flattening has been reported in numerous CV chondrites, such as Allende (Nakamura et al., 1995, 2000), Leoville (Cain et al., 1986; Nakamura et al., 1992), and Bali (Keller et al., 1994), and many CM chondrites (Lindgren et al., 2015; Tomeoka et al., 1999; Vacher et al., 2018). In experimental work on CM and CV chondrites, the preferred orientation foliation of flattened chondrules generated due to impact was perpendicular to the direction of impact (Nakamura et al., 1995, 2000; Tomeoka et al., 1999); the intensity of the preferred orientation increased with shock pressures up to 25 GPa; however, the foliation orientation began to deviate from this pattern at pressures above 25–30 GPa, and chondrule orientations became increasingly random (Tomeoka et al., 1999). Allende, with a shock classification of S1 (<5 GPa bulk pressure; Stöffler et al., 1991), has not been highly shocked, and therefore, we do not expect that it has been subjected to pressures above the 25 GPa threshold; therefore, the flattening of the chondrules and CAIs within Allende should provide a best estimate as to the direction of compaction.

Often, meteoritic components such as CAIs, chondrules, and matrix are considered in isolation of one another with respect to compaction, or not all components are considered as a collective (Forman et al., 2017, 2019; Keller et al., 1994; Nakamura et al., 1992, 1995; Rubin & Swindle, 2011) with the exception of a handful of studies (Forman et al., 2016; Lindgren et al., 2015; Tait et al., 2016). Here, we investigate compactional evidence from these three components in tandem, notably matrix, chondrules, and CAIs, at both the meso- and micro-scales, to determine if evidence of the compaction process is uniform across the different scales using crystallographic micro-scale techniques. As noted, the preferred orientations of CAIs and chondrules in Allende provide an excellent basis to decipher the probable direction of compaction according to the larger

components (chondrules, CAIs; Nakamura et al., 1995, 2000; Tomeoka et al., 1999). In this study, we also examine the crystallographic properties of the grains within the CAI and matrix grains across large areas, to obtain an understanding of collective directionality of compression as recorded by these much smaller meteoritic components. This is significant, as each meteoritic component can respond differently to the same compaction event (Bland et al., 2014; Davison et al., 2017) primarily relating to varying porosities (Bland et al., 2014) or strength. They may even record different events prior to the formation of planetary bodies, as in the case of some CAIs (Lorenz et al., 2019).

While modeling and prior analytical work demonstrated that heterogeneities are evident at the meso- and micro-scales (Bland et al., 2014; Davison et al., 2012, 2017; Forman et al., 2017), the use of large-area mapping here allows identification of large-scale fabrics and crystallographic trends, reducing the impact of minor heterogeneities on the analysis outcomes. In this study, we present the first use of large area electron backscatter diffraction (EBSD) analyses across a CAI in Allende and surrounding matrix at the micro-scale. We present crystallographic alignment analyses of matrices around two chondrules in the same section as the CAI, and re-analyze large area data from a study by Forman et al. (2017) to gain a wider understanding of crystallographic grain alignments using micro-scale techniques. Finally, we integrate our findings with meso-scale high-resolution photography of CAI elongation in Allende and consider the implications for early compaction processing across the three different scales.

MATERIALS AND METHODS

Macro-scale imaging of both sides of a flat cut polished 25 cm diameter slab of Allende was taken using a high-resolution digital camera at the National Museum of Natural History (NMNH) within the Smithsonian Institution, United States (Figure 1ai and bi). Image color thresholding was performed using the image processing software FIJI to highlight and characterize the shape and orientation of the cream-white elongate CAIs (Figure 1aii and bii). The elongate shape and light color of these features were used as identification of the CAIs over other features at this scale, such as chondrules. The orientation of the long shape axis of the fitted ellipse of each CAI was recorded from each side of the slice. CAI long shape axis ellipse orientations were compared to characterize the nature of any 2D shape-preferred orientations, and the results were displayed on rose diagrams using bins of 5° (Figure 1aiii and biii).

We used a 1-in. round thin section of Allende (WAM 13102, Western Australian Museum) for high-resolution electron microscopy analyses. This section was polished on a Buehler Vibromet II using 500 nm colloidal silica in NaOH for 4 h to create a reflective surface, and subsequently coated with ~5 nm of carbon to ensure electron conductivity under vacuum. Electron microscopy analyses were performed on a TESCAN Mira3 VP-FESEM in the John de Laeter Centre at Curtin University, Western Australia. EBSD was used to constrain the crystallographic orientation of the target grains at high resolution (100–250 nm step size). EBSD data were captured using 20 keV accelerating voltage and ~1.4 nA beam current at a working distance of 20.5 mm, and using an Oxford Instruments Symmetry CMOS EBSD detector. The Oxford Instruments Aztec system was used to direct the analysis of the sample and define the phases of interest for acquisition. A 1.6 mm × 0.5 mm cross section of an elongate type B calcium-aluminum-rich inclusion (CAI; MacPherson, 2014) was imaged via EBSD using a step size of 250 nm (identified in blue rectangle in Figure 2). Four additional 100 × 100 μm regions of the matrix surrounding this CAI were also imaged, at 100 nm step size (identified as blue boxes in Figure 2 as regions 1–4). Finally, seven 100 × 100 μm matrix regions around a rounded type IAB chondrule (C1, regions a–g in red boxes; Ushikubo et al., 2012) and eight 100 × 100 matrix regions around an elongate type IIAB chondrule (C2, regions a–h in orange; Ushikubo et al., 2012) were mapped at 100 nm step size. The small, high-resolution regions were analyzed to compare and contrast the matrix alignment around the different meteoritic components.

The data were noise reduced via a wildspike correction and a 6-point nearest-neighbor algorithm to remove erroneous data points, as is standard protocol for this type of data (Bestmann & Prior, 2003; Daly et al., 2019; Forman et al., 2016, 2017, 2019; Watt et al., 2006). Grains were identified based on an internal misorientation threshold of 10°, which is typical among EBSD studies such as those noted above, and reduced to a single representative point per grain to allow a data analysis unbiased by grain size. These points were collectively plotted onto lower hemisphere, equal area plots for olivine and clinopyroxene, and then contoured with a half width of 15° and a data clustering of 5° to identify crystallographic preferred orientations (CPOs).

This particular thin section (WAM 13102) was the focus in a prior study (Forman et al., 2017), and the previously explored region is highlighted in Figure 2 in yellow for contextual purposes. The outcomes of re-analyzing that data are reviewed here; due to improvements in data processing and computing power, it was possible to plot all matrix grains from the 2 mm × 6 mm area on a single lower hemisphere, equal area plot for olivine, which was then contoured with the same specifications as above. As in Forman et al. (2017),

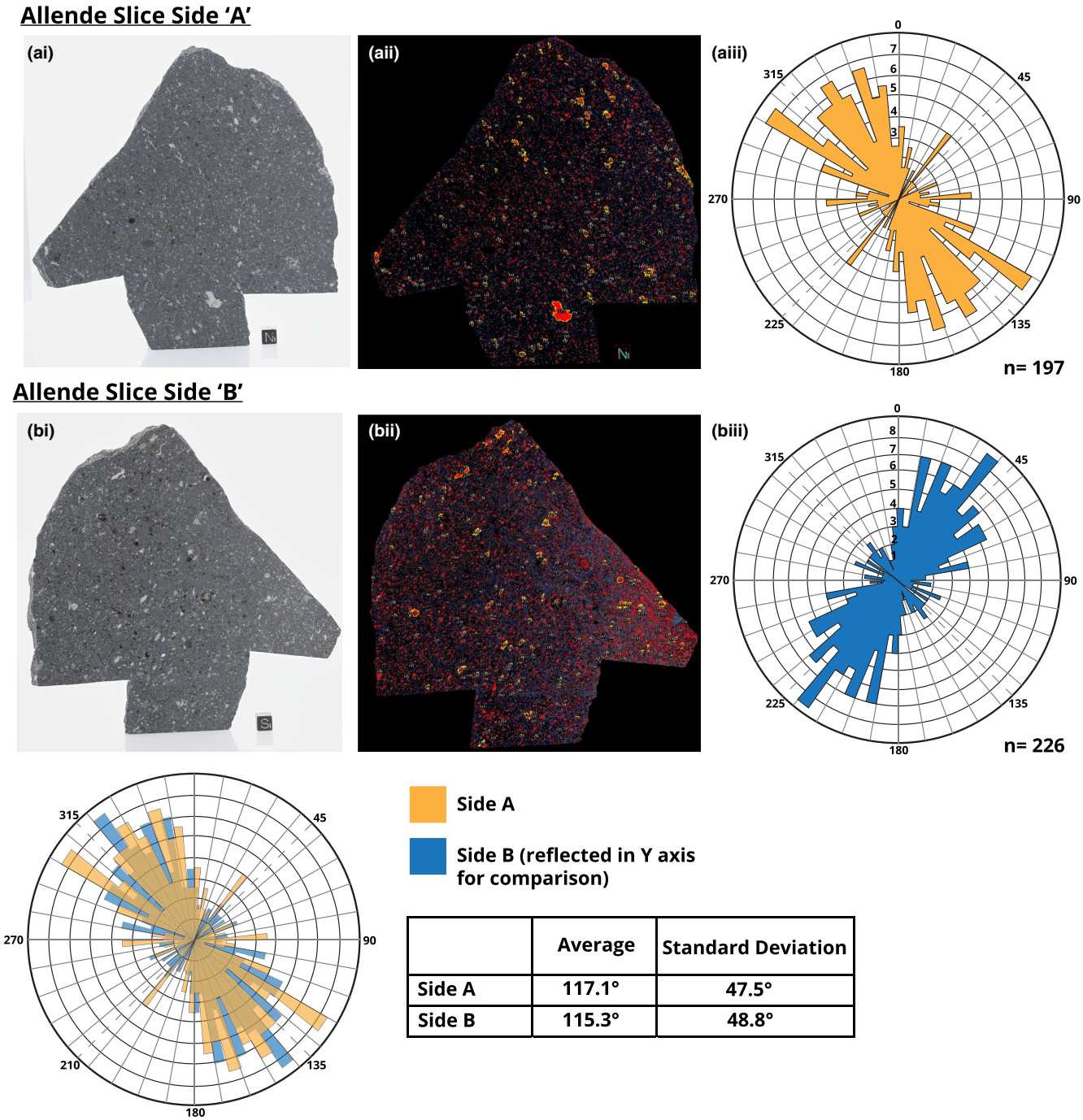

	Average	Standard Deviation
Side A	117.1°	47.5°
Side B	115.3°	48.8°

FIGURE 1. i) High-resolution photographs of a slab of the Allende meteorite, taken at the Smithsonian Institution (a and b are the two sides of the same slab), ii) color-thresholded images of the slabs to highlight the creamy-white calcium-aluminium inclusions (CAIs) on each side, iii) rose diagrams showing the orientations of the long axis of fitted ellipse for all CAIs. (Color figure can be viewed at wileyonlinelibrary.com.)

only the olivine matrix grains three times the step size in circle-equivalent diameter (0.5 μm in the aforementioned data set) were analyzed to ensure data quality and sufficient sampling of each grain included in the study for robustness. Previously used SEM conditions are outlined in Forman et al. (2017).

RESULTS

Meso-Scale CAI Analyses

Chondrule and CAI alignments have been documented previously by many studies (Keller et al.,

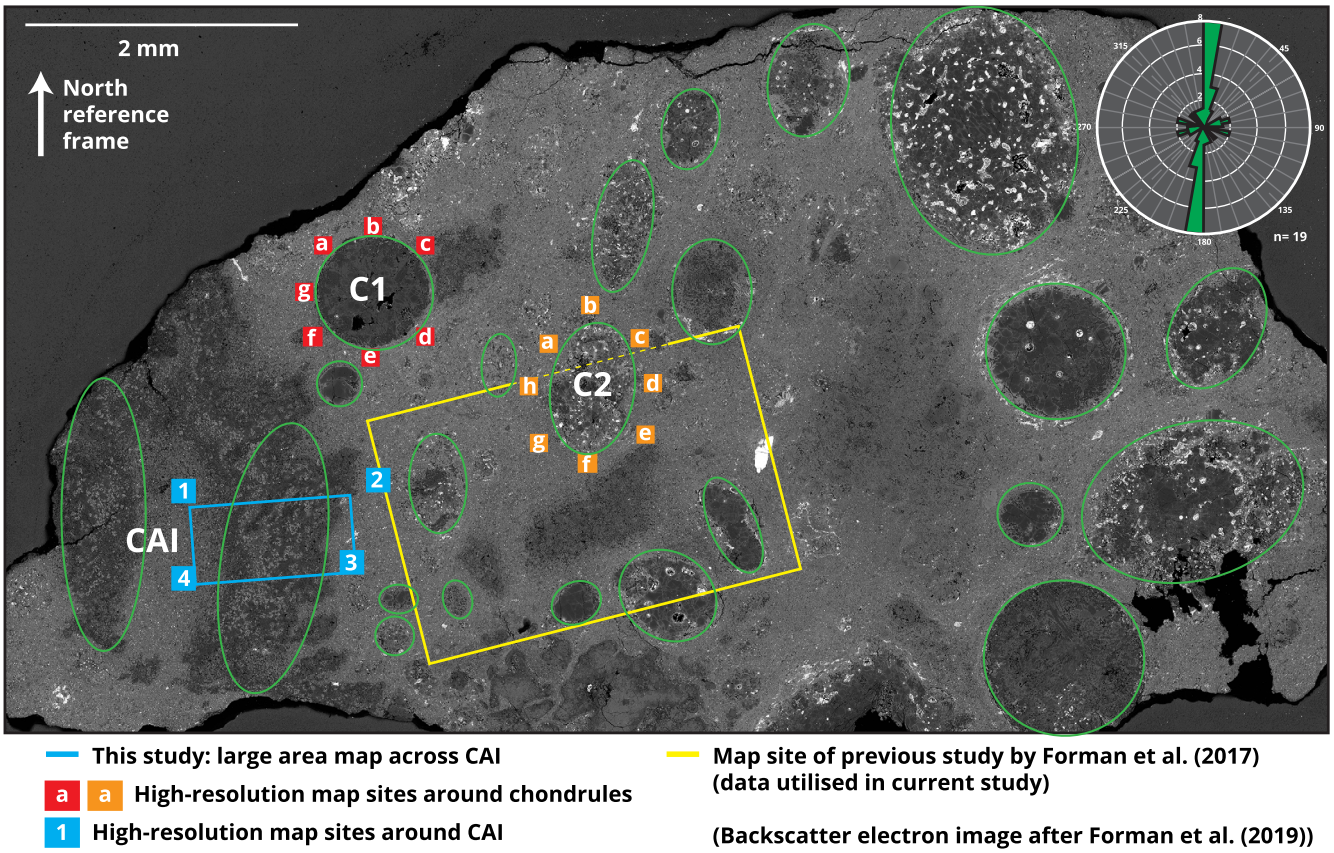

FIGURE 2. Overview backscatter electron (BSE) image of Allende thin section (WAM 13102) adapted from Forman et al. (2019). Regions highlighted in red indicate data collected in this study, and region highlighted in yellow indicates the location of large area mapping data collected in Forman et al. (2017). Red rectangle indicates the location of the LAM collected including the calcium-aluminium inclusion (CAI). Regions noted with letters a–h are the locations of high-resolution maps collected surrounding chondrules C1 and C2, and regions numbered 1–4 are the locations of high-resolution maps around the CAI under study. Best-fit ellipses in green highlight the approximate orientations of the CAIs and chondrules that are readily identifiable. A rose diagram is shown to demonstrate the relative constancy in ellipse elongation orientation in this section, similar to the trend at the macro-scale seen in Figure 1. (Color figure can be viewed at wileyonlinelibrary.com.)

1994; Lindgren et al., 2015; Nakamura et al., 1992, 1995, 2000; Rubin & Swindle, 2011; Scott et al., 1992; Tait et al., 2016; Tomeoka et al., 1999; Vacher et al., 2018), and therefore, Figure 1 is shown purely to demonstrate the constancy of the elongate CAI orientations in Allende. Both sides of the photographed slab were analyzed here (Figure 1ai and bi); a total of 423 CAIs were detected and assigned a best-fit ellipse (Figure 1aii and bii); and the orientations of the long axis of the ellipses were plotted onto rose diagrams (Figure 1aiii and biii). Both sides of the slab demonstrate palpable 2D CAI-preferred orientations; both sides have a corrected average orientation between 115° and 120° and a standard deviation of 47°–49°. While there is a spread in CAI orientation statistically, the trend is clear and consistent.

Chondrules and CAIs examined within the thin section of Allende demonstrate relative constancy in the orientation of elongation (~N-S), with some outliers (Figure 2). Based on our findings using macro-scale photography, we will assume this trend in CAI and chondrule elongation orientation would be consistent at a larger scale for the purpose of this study. All directional measurements from this point forwards will be described in relation to the reference frame of Figure 2, which is noted via a N arrow in each figure.

Micro-Scale Crystallographic Analyses

Large Area Mapping: Matrix Grains

The previously examined region in this section from Forman et al. (2017) is identified in the backscatter electron (BSE) SEM image in Figure 2 in yellow and in higher resolution as an EBSD phase map in Figure 3a; due to enhancements in data processing software and general computing capability, here we re-examine the data of 304,194 olivine grains collectively on a single

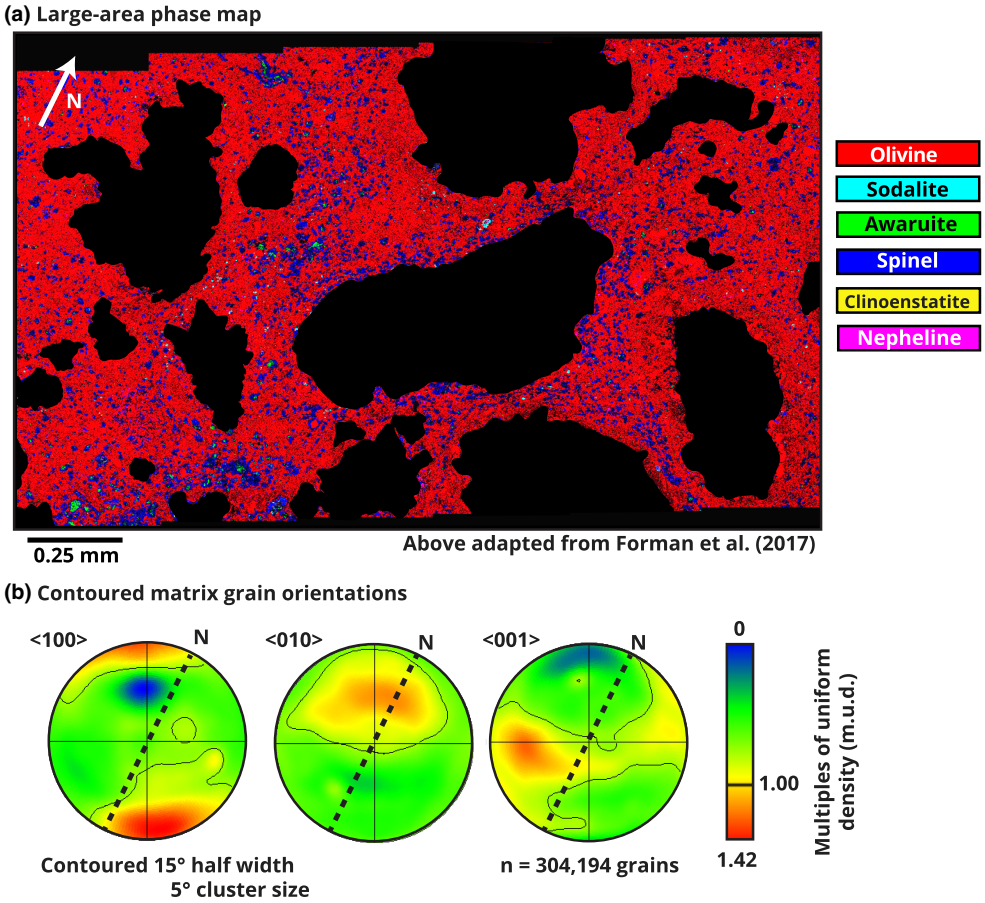

FIGURE 3. a) Large area matrix phase map collected by Forman et al. (2017); phases defined by crystallographic measurements, b) lower hemisphere, equal area plot displaying contoured crystallographic orientations of 304,194 matrix grains from the large area map. The data were contoured with a half width of 15° and a cluster size of 5°. (Color figure can be viewed at wileyonlinelibrary.com.)

lower hemisphere, equal area plot (Figure 3b), to identify the principal fabric over the 2 × 4 mm area. Previously, this region was analyzed in segments in a grid system to understand heterogeneities in fabrics or CPOs (Forman et al., 2017).

The strength, pattern, and orientation of the collective CPO can be characterized. The strength of the CPO is measured in multiples of uniform density (m.u.d.). Here, the maximum m.u.d. within this large area is low (defined as low m.u.d. = 1–2; moderate m.u.d. = 2–3; high m.u.d. = 3+ in this study) and measures only 1.42, where 1.00 represents a random fabric. The pattern, however, is clear; the <100> axis forms a point maxima CPO (whereby many instances of <100> plot in a cluster on lower hemisphere, equal area plots) oriented NNW–SSE and in the plane of the sample (Figure 3) in relation to the reference frame of Figure 2. The <010> axis forms a more diffuse point maxima, at approximately 90° to the <100> axis. The <001> axis forms a weak girdle maxima (where <001> data points lie on a great circle when plotted on lower hemisphere, equal area plots) where <001> is oriented in the ENE–WSW plane relative to reference frame of Figure 2 (Figure 3).

Large Area Mapping: CAI and Surrounding Matrix

The large area map (LAM) of a cross section of a CAI in Allende is shown in Figure 4. Figure 4a shows the BSE map defining the edge of the CAI, and Figure 4b shows the phase map of the region, as detected by crystallography. The matrix regions surrounding the CAI are predominantly olivine (Figure 4b) with small blebs of clinopyroxene included. The CAI is composed almost exclusively of clinopyroxene with some minor amounts of perovskite, spinel, and melilite throughout. At the CAI rim, spinel is abundant and is more dominant in the western edge, creating a diffuse CAI boundary.

The crystallographic orientations of all olivine matrix grains on either side of the CAI and clinopyroxene grains within the CAI were assessed separately (Figure 4ci–iii). Matrix olivine grains to the west of the CAI (n = 19,751; Figure 4ci) collectively show a weak point maxima in <100> oriented perpendicular to the edge of the CAI in

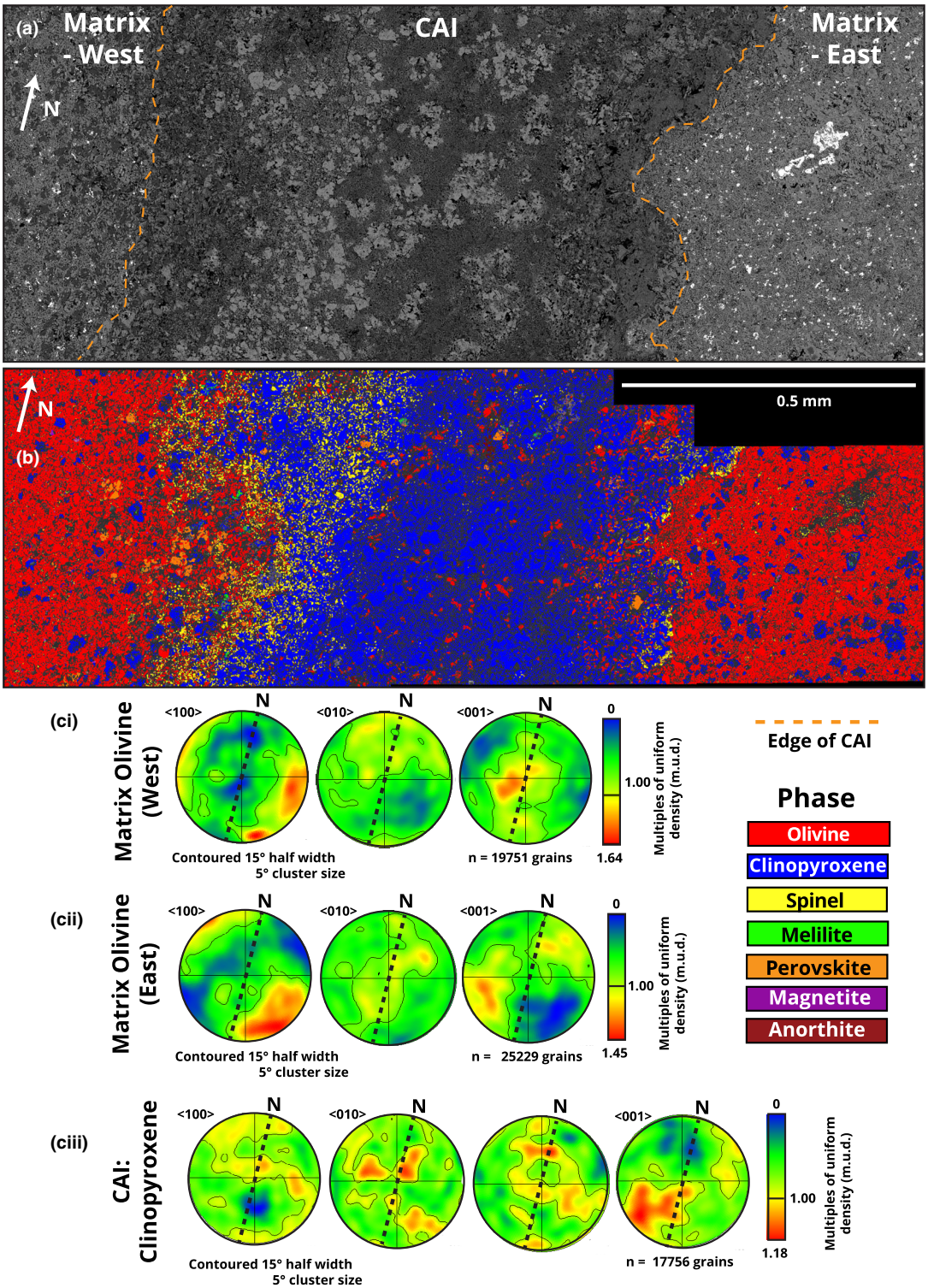

FIGURE 4. a) Backscatter electron (BSE) image of the calcium-aluminium inclusion (CAI) cross section. The dotted orange line denotes the edge of the CAI and the start of the matrix, b) large area phase map, defined by crystallographic measurements, of cross section of CAI, c) contoured lower hemisphere, equal area plots of i) matrix grains to the west of the CAI in the plane of this sample, ii) matrix grains to the east of the CAI, and iii) clinopyroxene grains within the CAI. All data were contoured with a half width of 15° and a cluster size of 5°. (Color figure can be viewed at wileyonlinelibrary.com.)

the E–W orientation, and a very weak point maxima in <001> oriented perpendicular to the plane of the sample and parallel to the suspected edge of the CAI if the edge were to continue in the third dimension throughout the sample. Matrix olivine grains to the east (n = 25,229; Figure 4cii) also show a weak point maxima in <100> oriented perpendicular to the CAI edge (when considering the curved shape of the CAI boundary) in the NW–SE orientation, and a very weak girdle maxima in <001> oriented approximately parallel to the CAI edge in the NE–SW orientation.

The clinopyroxene grains in the CAI were considered collectively; while both diopside and fassaite varieties are present, crystallographically the two phases are difficult to consistently distinguish by EBSD at this resolution. As their crystal systems are identical, the two-phase data sets were merged. Grains within the CAI present the weakest observable CPO of all regions in this section (Figure 4ciii); the maximum m.u.d. (1.18) is generated by the very weak point maxima in <001>, oriented toward the SSW of the sample, and parallel with the long shape axis of the CAI. No discernible patterns are present in <100> or <010>.

High-Resolution Mapping: Matrix Regions Around CAI [1–4]

Four 100 × 100 μm matrix regions at the edge of the LAM described above were assessed for the presence and nature of any CPOs in the matrix olivine grains (Figure 5) to identify any variations along the edges of the CAI, owing to the observed curved edge. The BSE map in the center of Figure 5 shows the edges of the CAI clearly; to the east of the BSE map, the two mapped regions (regions [2] and [3]) both display weak point maxima in <100> (max. m.u.d. of 1.92 and 1.96, respectively) oriented perpendicular to the edge of the CAI in the SE–NW orientation. Region [2] demonstrates a very weak girdle maxima in <010> (max. m.u.d. of ~1.20), oriented parallel to the edge of the CAI in the NE–SW orientation. Region [3] also displays a very weak and diffuse point maxima in <001>. To the west of the CAI, region [1] displays a moderate point maxima in <100> oriented approximately perpendicular to the edge of the CAI in the NE–SW orientation and a very weak girdle maxima in <001> oriented approximately parallel to the edge of the CAI and at 90° to <100> in the NW–SE orientation. Region [4] displays diffuse point maximas in both <100> and

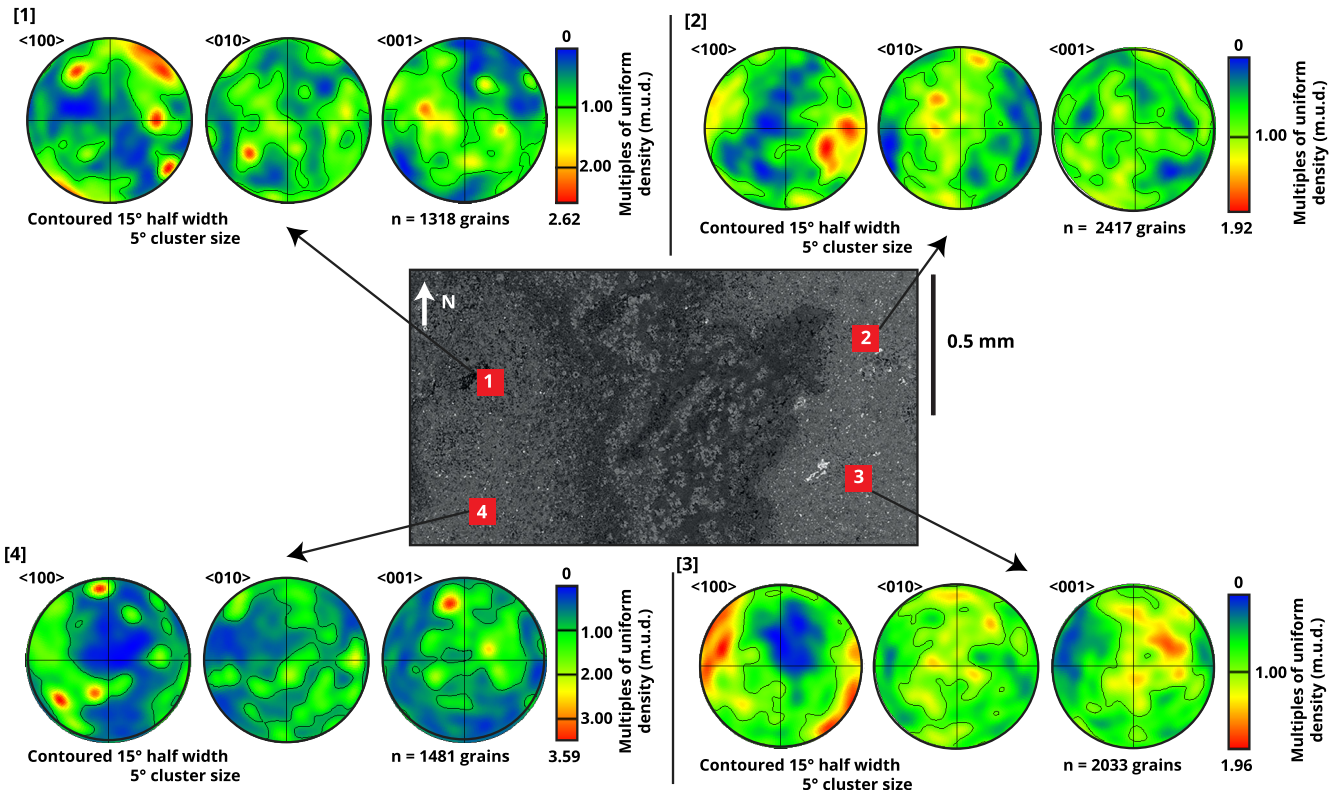

FIGURE 5. Contoured lower hemisphere, equal area plots from high-resolution maps surrounding the calcium-aluminium inclusions [1–4]. All data were contoured with a half width of 15° and a cluster size of 5°. Center reference image is backscatter electron map, adapted from Forman et al. (2019). (Color figure can be viewed at wileyonlinelibrary.com.)

<001>; <100> is oriented approximately perpendicular to the edge of the CAI; and < 001> is oriented pointing out of the plane of the sample. In each case regardless of the strength of the CPO, the <100> of the olivine grains is consistently oriented perpendicular to the edge of the CAI. The number of grains measured within each region is all statistically significant; however, the regions to the west have fewer grains recorded. This could be due to a greater number of accessory mineral grains being present, smaller grain sizes and therefore fewer grains were included following removal of grains too small to be sufficiently sampled due to step size, larger grains and therefore fewer in the region of interest, or a higher porosity to the west.

High-Resolution Mapping: Matrix Around Chondrules

Seven (C1) and eight (C2) matrix regions surrounding two chondrules (C1 and C2) were analyzed (Figures 6 and 7, respectively). BSE maps of the chondrules and surrounding matrices are displayed in the center of Figures 6 and 7, and the collective crystallographic data within each matrix region around C1 ([a]–[g]) and C2 ([a]–[h]) are also displayed.

Chondrule 1 (C1)

CPOs are present within the olivine grains in most matrix regions that were analyzed surrounding this chondrule (Figure 6). The strength of the CPOs (measured via maximum m.u.d. values) varies from weak ([b]-1.97 and [f]-1.88) to moderate–strong ([d]-4.36). The moderate CPOs are regions [a], [c], [e], and [g]; therefore, the most strongly aligned regions lie ESE and WNW of the chondrule. In terms of the nature of the CPOs, the <100> axis forms a clear point maxima in six of the regions ([b]–[g]); out of these, <100> is oriented perpendicular to the chondrule edge in three regions ([b] and [d]–[e]) and subparallel to the chondrule edge in two regions ([c] and [g]). Girdle maximas in <001> are present in the same aforementioned five regions and these are oriented parallel ([b] and [d]–[e]) or subparallel ([c] and [g]), to the chondrule edge. The clearest incidence of this pattern is found in region [d]. The two regions which have <001> axes subparallel to the chondrule edge ([c] and [g]) demonstrate the same trends in orientation of axes alignment. Region [f] does not follow the same trend as the other regions, whereby <100> forms a point maxima but appears oriented parallel to the chondrule edge. Region [a] does not display any discernible CPO patterns.

Chondrule 2 (C2)

As for C1, CPOs can also be identified within the matrix olivine grains around C2 (Figure 7). Although weak–moderate in magnitude, the strongest CPOs (measured via maximum m.u.d.) are regions [a], [d], [e], [f], and [h] (m.u.d. values 2.10 ([a])-2.75 ([e] and [h])), which lie SE and WNW of the chondrule. Regions [a], [d],

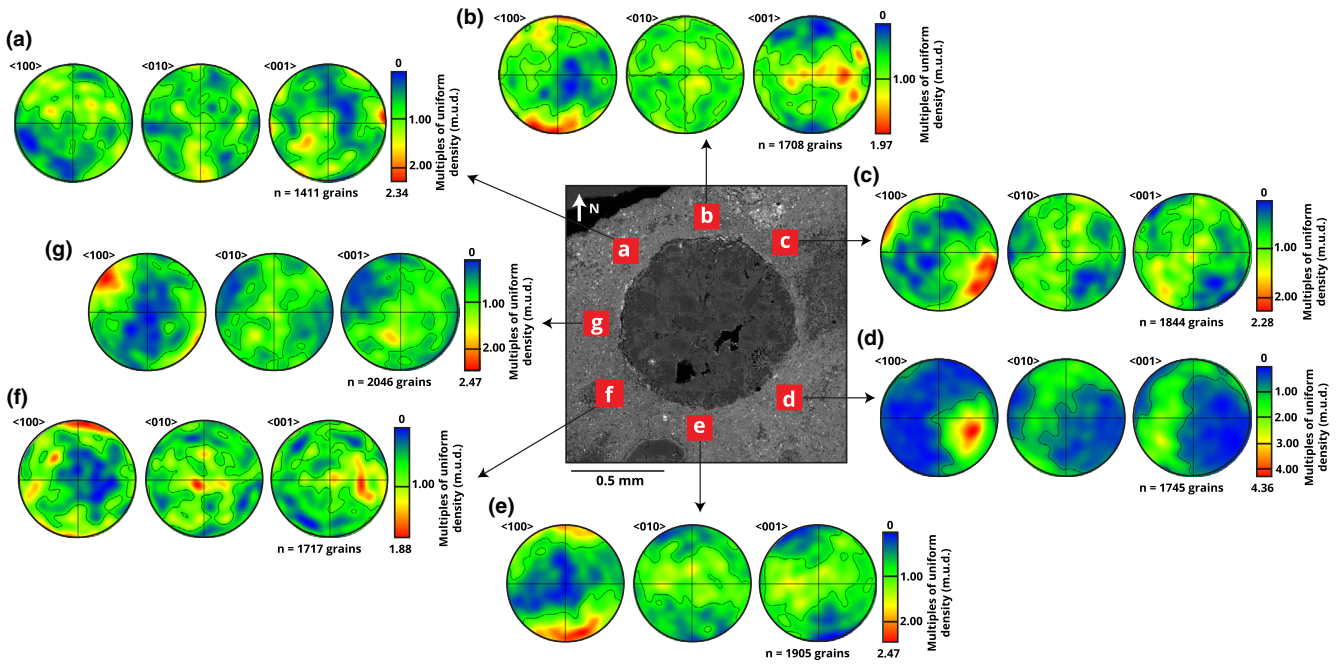

FIGURE 6. Contoured lower hemisphere, equal area plots from high-resolution maps surrounding the chondrule C1 [a–g]. All data were contoured with a half width of 15° and a cluster size of 5°. Center reference image is backscatter electron map, adapted from Forman et al. (2019). (Color figure can be viewed at wileyonlinelibrary.com.)

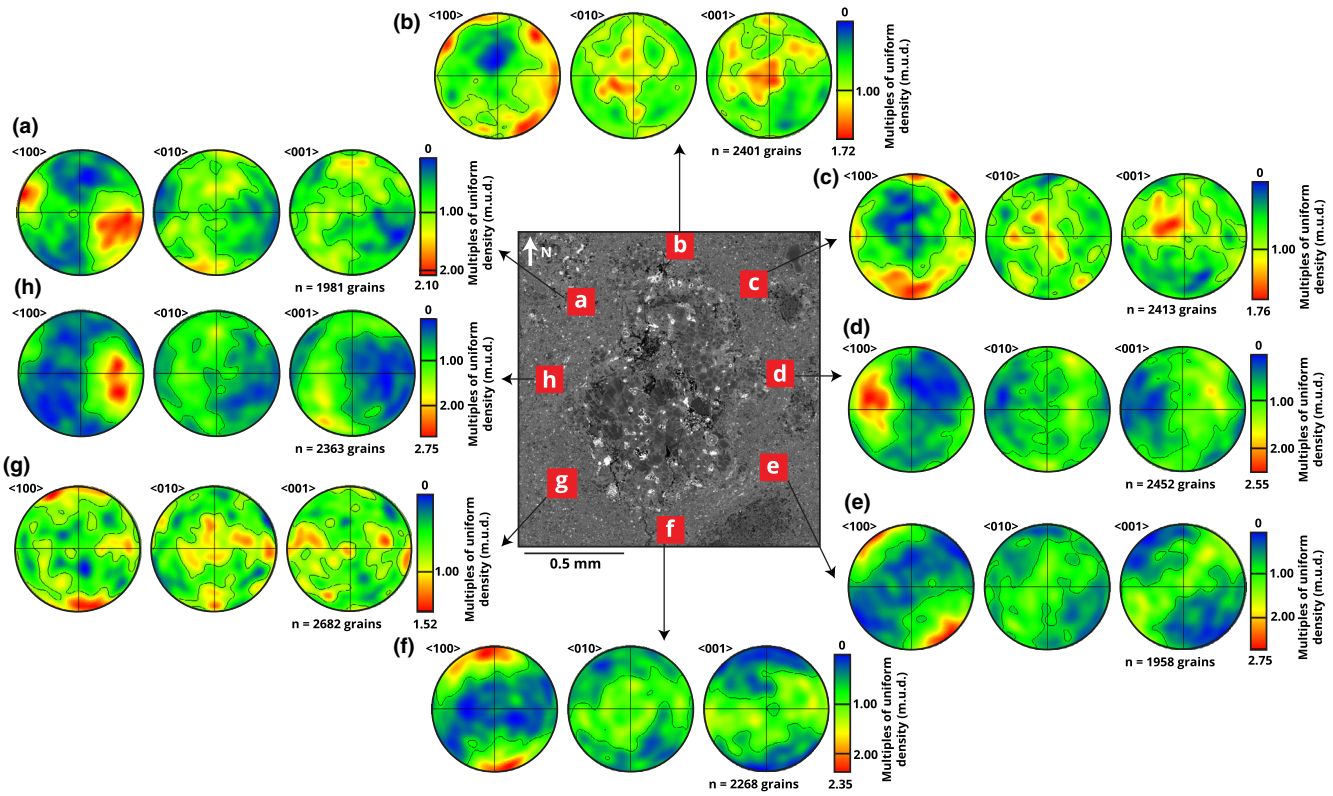

FIGURE 7. Contoured lower hemisphere, equal area plots from high-resolution maps surrounding the chondrule C2 [a–h]. All data were contoured with a half width of 15° and a cluster size of 5°. Center reference image is backscatter electron map, adapted from Forman et al. (2019). (Color figure can be viewed at wileyonlinelibrary.com.)

[e], [f], and [h] all have a point maxima in <100> oriented perpendicular to the chondrule edge, and girdle maximas in both <010> and <001> oriented parallel to the edge of the chondrule. Region [g] displays a very weak point maxima in <100>, oriented parallel to the chondrule edge. Regions [b] and [c] have point maximas in <001>, oriented perpendicular to the plane of the sample, and potentially parallel to the edge of the chondrule if the chondrule continued in the third dimension.

DISCUSSION

The synthesis of all results from thin section analyses is shown in Figure 8. Fabrics or CPOs are observable at all scales investigated in this study, whereas their nature and orientation vary across the scales and between regions.

Petrofabric Analysis

CAIs and Chondrules

Using the knowledge that there is minor spread in CAI orientations across this meteorite (Figure 1), we were able to confidently identify a prominent elongate CAI for microscopic analyses that is approximately aligned with other elongate features (other visible CAIs, chondrules, and inclusions; Figures 2 and 8.1). The orientation of the elongate axis of the CAI we examined is therefore likely representative of the macroscale alignment seen on the slab in Figure 2, and our microscale measurements can be considered in the macroscale context that this provides. Here, the majority of meso-scale components are elongate in the general N–S orientation with some clear anomalies, that is, some chondrules that are aligned perpendicular to this general trend (Figure 8.1). This elongation of chondrules and CAIs is interpreted to result from compaction via impact, as has been found in many prior studies (Keller et al., 1994; Nakamura et al., 1992, 1995, 2000; Scott et al., 1992; Tait et al., 2016).

The grains within the CAI demonstrate only a very weak point maxima long-axis CPO in <001>, which implies a weak lineation roughly along the length of the CAI (Figure 4). This is distinctly different from the nature of the matrix CPOs at all sites, which demonstrate flattening textures. Lineations are often generated by processes such as flow (Bhattacharyya, 1966; Daly et al., 2019; Lezzi & Ventura, 2002; Merle, 1998) and are

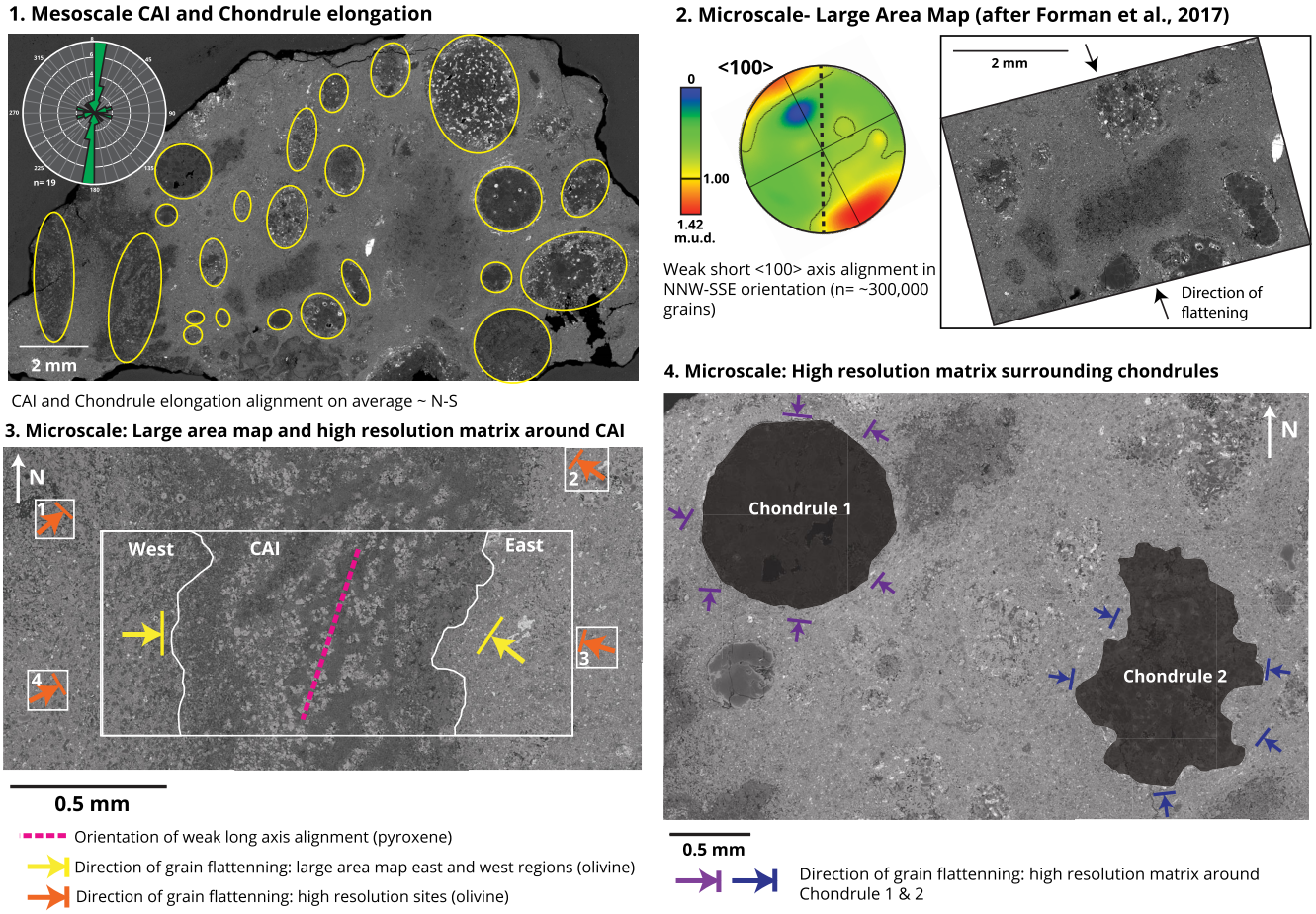

FIGURE 8. Synthesis of all meso-scale and micro-scale orientation information gathered across this section of Allende; 1) best-fit ellipse assigned to all chondrules and calcium-aluminium inclusions (CAIs) observable in the section. Long axes form a relatively consistent N–S trend, indicative of shortening and therefore compression in the E–W orientation; 2) microscale, contoured lower hemisphere equal area plot of matrix from LAM after Forman et al. (2017) and corresponding BSE map of the measured area. Corrected orientation of the lower hemisphere plot indicates compression in the NNW–SSE orientation according to the crystallographic orientations across 304,194 olivine matrix grains; 3) BSE image of CAI and surrounding matrix regions, including the region of the LAM of the CAI, and four surrounding high-resolution matrix grain sites. Arrows and lines (yellow and orange) demonstrate the orientation of the short axis of the olivine matrix grains, and the pink dotted line indicates the orientation of the weak lineation formed by the pyroxene grains within the CAI. All high-resolution matrix sites indicate compression against the CAI edge, which is variable (NNW–SSE, SSW–NNE, and E–W) while the lineation in the CAI indicates a "flow" along the length of the CAI; 4) BSE image of the two chondrules (C1 and C2) and the surrounding matrix regions that demonstrate an observable crystallographic preferred orientation. Matrix grains are predominantly flattened against the chondrule edges and are strongest situated to the SE and NW of the chondrules. We use this to infer the orientation of compression to be NW–SE as determined from the high-resolution matrix grain sites. (Color figure can be viewed at wileyonlinelibrary.com.)

unlikely to be caused by pure compaction-related processes. However, the shape of CAIs within Allende forms a lineation in 3D (Tait et al., 2016). CAIs are noted to be the least resistant chondritic feature via strain analysis compared with chondrules and matrix, and consequently appear the most deformed (Tait et al., 2016). As this CAI is fine grained, it was likely to have its own porosity which would have been filled first, allowing for the CAI to compact and deform similar to some chondrules studied from the CM chondrite Murchison (Hanna et al., 2015). Once the porosity has been removed, Tait et al. (2016) surmised that CAIs will "flow" into nearby pores of the surrounding matrix regions. This lineation may be evidence of this process, which implies the internal CAI fabric could be driven by compressive forces.

Matrix Grains

At the microscale, there is a relatively consistent trend in the nature of the CPOs across the section. The >300,000 matrix grains from the LAM first published in Forman et al. (2017) present a <100> point maxima,

based on the NNW–SSE orientation of the <100> CPO, and the same girdle maxima in <001>, perpendicular to <100> (Figure 3), that is seen in many other regions across this sample. Figures 4–6 demonstrate that most 100 μm × 100 μm matrix grain sites around each chondrule (C1, C2, Figures 5 and 6, respectively) and the CAI (Figure 4) demonstrate point maximas in <100> that are oriented perpendicular to the component edge. In addition, many of the same sites demonstrate a girdle maxima in <001>, oriented parallel to the edge of the component. While the absolute orientations are variable, the orientation relationship of the matrix grain CPOs and larger meteoritic components is very similar.

Observations by Forman et al. (2019) and Watt et al. (2006) have shown that <100> is the shortest physical dimension of the olivine matrix grains in Allende, and <001> is the longest dimension. Consequently, at all sites where the point maxima in <100> or the girdle maxima in <001> is observed, the matrix grains collectively demonstrate a flattening CPO, either compressed in a specific absolute orientation or compacted against a chondritic component; regardless, the driver is compression. We therefore interpret the orientation of the <100> axis to be the direction of compaction. This flattening CPO is consistent with previous observations within Allende and is in agreement with the evidence of flattening observed from meso-scale components (Bland et al., 2011; Forman et al., 2016, 2017; Muxworthy et al., 2017; Nakamura et al., 2000; Scott et al., 1992; Tait et al., 2016; Watt et al., 2006).

Orientation of Compression

Experimental impact results demonstrated that chondrule-like components generally flatten perpendicular to the axis of compression (Nakamura et al., 1995, 2000) at low pressures (<25 GPa; Tomeoka et al., 1999). Here, the general orientation of the long axis of meso-scale components is ~N–S (Figure 8.1), which is consistent with an ~E–W axis of compression.

The orientation of the internal CAI lineation fabric in relation to the overall shape of the CAI is in agreement with the "flow"-like process suggested by Tait et al. (2016); the long axis (<001>) of the grains would align with the direction of flow, that is, along the resultant long edge of the CAI, and consequently perpendicular to the direction of compression. As the elongation of the CAI is concurrent with the elongation of other meso-scale features, it stands that the lineation observed is approximately perpendicular to the direction of compression. We therefore interpret this lineation to be driven by the same compressive forces as the flattening fabrics seen in the chondrules.

Matrix regions imply a variety of compaction orientations. The LAM, re-analyzed after Forman et al. (2017), indicates compression in the NNW–SSE orientation (Figure 8.2). Olivine matrix grains within the LAM around the CAI to the east (Figures 4 and 8.3) are consistent with compression in the NW–SE orientation, and grains to the west are consistent with E–W compression orientation (Figure 8.3). The asymmetry of the matrix CPOs around C1 [a–g] and C2 [a–h] can be further used to infer the direction of compression; the strongest CPOs are broadly found to the SE and NW of the chondrules; and as these are flattening CPOs, this coincides with compression in the NW–SE orientation (Figure 8.4). Finally, the high-resolution sites to the west and east of the CAI indicate compression in the NE–SW and NW-SE orientations, respectively (Figure 8.3). Here, we note that as most point maxima CPOs appear in the plane of the sample (i.e., are displayed close to or at the edge of the lower hemisphere equal area plots), we can consider the compression directions within this plane.

Petrofabric Origin on the Allende Parent Body

There are clear differences in the orientation of the CPOs and inferred directions of compaction at the different scales (Figure 8); at the meso-scale, broadly E–W with some variation; collective matrix at the LAM microscale indicates compression NNW–SSE; matrix at high-resolution sites around chondrules and within the LAM east of the CAI indicate compression in the NW–SE orientation; and high-resolution matrix regions to the west of the CAI indicate compression in the NE–SW. This demonstrates a variation in compaction direction of approximately 125°, but this is not inconsistent with an impact-driven compaction model.

Single, High-Intensity Impact

Firstly, considerations must be made for the possibility of heterogeneities within the matrix as the cause for differing chondrule/CAI and matrix compressional records from a single, high-intensity impact event (Bland et al., 2014; Davison et al., 2016; Forman et al., 2017). Matrix is known to record heterogeneities of shockwave interactions that may not be detected when examining larger components such as chondrules (Bland et al., 2014; Davison et al., 2014, 2016, 2017; Forman et al., 2016, 2017). Fine-grained matrix regions are highly porous, especially when compared with non-porous or low-porosity chondrules, and during impacts, the pore spaces collapse, creating temperature and pressure excursions (Bland et al., 2014; Davison et al., 2016), which allow for grain realignment and deformation in response to the compressional force. While it is possible that a single impact event could generate similar orientation variation within the matrix as seen here (Bland et al., 2014), it is improbable that this

meteorite was only affected by a single, porosity-reducing impact while on the CV parent body. Other planetary bodies are predicted to have undergone multiple impacts (Lindgren et al., 2015) and impacts are very common throughout the evolution of our solar system.

The shock stage of Allende –(S1; Scott et al., 1992) is inconsistent with a high-intensity impact scenario. The large reduction in matrix porosity from the predicted starting material (~70% pre-compacted matrix porosity; Bland et al., 2014), 26% matrix porosity now (Nakamura et al., 2000) necessitates a relatively high-intensity impact be responsible if only one impact has affected the Allende sample. Minimal shock features, and the lack of traditional shock markers such as melting and fracturing, imply that Allende did not experience greater than 5 GPa of peak pressure during impact, and limited heating is evident within the sample. Furthermore, experimental impacts using Allende as the starting material demonstrated that pressures of 11–21 GPa progressively generated less porosity and greater degrees of chondrule flattening (Nakamura et al., 2000). The average aspect ratio of chondrules in Allende is 1.10 (Nakamura et al., 1995, 2000), which is consistent with very low shock pressures (Scott et al., 1992; Stöffler et al., 1991). Consequently, the evidence does not support a high-intensity impact scenario.

Heterogeneities arising from a single impact are likely to be inconsistent across large areas (Bland et al., 2014; Davison et al., 2014, 2016, 2017; Nakamura et al., 2000). The CPOs measured within the high-resolution matrix regions here are not simply random; there is an observable pattern consistent with a different compression direction to the meso-scale features. Predictions from the modeling of Bland et al. (2014) determined that matrix variations, in terms of heating and pressure excursions, coincide with the direction of shockwave propagation; regions on the lee side of chondrules would be shielded from the effects of the shockwave; and matrix regions on the opposite side would experience amplified temperature and pressure excursions. If we use CPO presence and strength as an indicator for relative temperature and pressure excursions within the sample, our results are therefore consistent with a compression in the NW–SE orientation (Bland et al., 2014), which is inconsistent with the compression orientation implied by the meso-scale features.

We note that high-resolution matrix regions around the chondrules and CAI demonstrate localized fabrics against the closest resistant chondritic object. CPO heterogeneities can arise within the matrix dictated by the relative location and distance to nearby resistant objects (Forman et al., 2017; Watt et al., 2006), and also are dependent on the competence of said "resistant" objects; the CAIs in Allende demonstrate the greatest degree of shortening and strain partitioning when compared with matrix and chondrules (64.4% vs. 21.5% vs. 17.6%, respectively; Tait et al., 2016). It therefore follows that matrix CPOs around the CAI may be expected to be related more closely to the orientation of the attenuating compressive shockwave, rather than the location with respect to the CAI edges. However, the matrix CPOs here are aligned approximately with the edge of the CAI but are much weaker than matrix CPOs seen elsewhere. This suggests that matrix CPO orientations around CAIs are a combination result from both the orientation of shockwave attenuation and the relationship to the CAI edges. Around chondrules, which are much more resistant to shortening owing to the lack of porosity and mineralogy (Tait et al., 2016), matrix is likely to exhibit much stronger CPOs that are closely related to the shape of the chondrule edge closest to the region, rather than the absolute orientation of the attenuating shockwave. However, here we have employed asymmetry relationships to deduce the orientation of the compression shockwave.

The examination of matrix regions at different scales and over small and large areas have all yielded different results to the meso-scale components. The purpose of measuring a large number of grains over the LAMs was to mitigate the effects of CPO heterogeneities (Forman et al., 2017), which was successful. Regardless, in many cases, the microscale high-resolution mapped areas surrounding the chondrules are approximately in agreement with the orientation of compression as suggested by results from the microscale LAM data. This suggests that the matrix regions collectively record a different compression direction to the meso-scale features based on orientation of compaction measurement criteria. We consequently deem it unlikely that matrix heterogeneities arising from a single impact could have produced the observable CPO configurations.

Multiple Impacts

We next consider the potential that multiple impact events occurred at different orientations. As noted in many studies (Bland et al., 2011, 2014; Nakamura et al., 1995, 2000; Rubin & Swindle, 2011; Scott et al., 1992), the larger components, such as chondrules and CAIs, would have flattened when the matrix was still highly porous. We, therefore, predict that compression occurred in the E–W orientation to flatten and align the meso-scale components during one of the earliest compression events. After this point in time, it is possible that the matrix retained some of its porosity; Allende does not exhibit evidence of high-pressure impact events that could reduce the porosity to the currently observed porosity in a single event (Nakamura et al., 1995, 2000; Scott et al., 1992). The matrix likely, therefore, records evidence of subsequent gentle compactional events at slightly different orientations. Impact experiments using

Allende as the starting material found that with increased impact pressures, the material had lowered matrix porosities and higher aspect ratios of the chondrules (Nakamura et al., 2000). These experimental pressures are higher than Allende has experienced (11–21 GPa experimentally; Nakamura et al., 2000), compared to <5 GPa for Allende (Fritz et al., 2017; Scott et al., 1992) and consequently porosity is highly likely to have been preserved following the initial chondrule-flattening impact event and subsequent impacts. Impact compaction modeling demonstrated that single impacts at speeds over 3 km s^{-1} generated widespread melting due to collapse of pores in initially highly porous media (Bland et al., 2014); such melting is not observed in Allende; further supporting that multiple, gentle impacts were the driver of parent body compaction.

Matrix grain CPOs shown here formed in response to the direction of compaction (e.g., Figure 3) or flattened according to the angle at which the nearest component edge was situated (e.g., Figures 4–8). The high-resolution regions around chondrules and CAIs, and the large area mapped region of matrix, indicate compression in the NW-SE and NNW–SSE/NNE–SSW orientations, respectively, which is approximately 125° at maximum from the inferred compression based on meso-scale observations. If we consider Allende's location on the CV parent body, a variation of up to 125° in shockwave propagation direction is conceivably achieved by different impacts on the parent body surface. Allende experienced temperatures of up to ~600 K on the parent body (Bonal et al., 2006), implying the sample originated from some depth in order to reach these temperatures during thermal metamorphism. Investigations into the CV3 Kaba used the magnetization of the sample to infer the depth of the sample on the parent body. In lieu of any such approximation in the literature for Allende, we used the depth inferred for Kaba, which was predicted to be 2–4 km (Dodds et al., 2021). It is clear from this approximation, shown in Figure 9, that impact events, gentle in nature as is dictated by the lack of shock features within the sample, likely propagated to the location of Allende from only one side of the parent body generating hemispheric shock features. This could easily generate the variation in compaction orientation across the different scales shown here, where matrix porosity remained after the initial impact that compacted and oriented the chondrules and CAIs.

The process of accretion of all planetary bodies involves the collision and assimilation of planetary materials (Agnor & Asphaug, 2004; Weidenschilling, 2019; Weidenschilling & Cuzzi, 2006). We have considered the effects of impacts into the parent body when the CV parent body had mostly accreted, however as impacts are involved in the process of accretion of asteroids, our observations may record evidence of inter-accretion impact events. This would mean it is highly likely that Allende would demonstrate evidence of impacts from different locations/directions as the CV

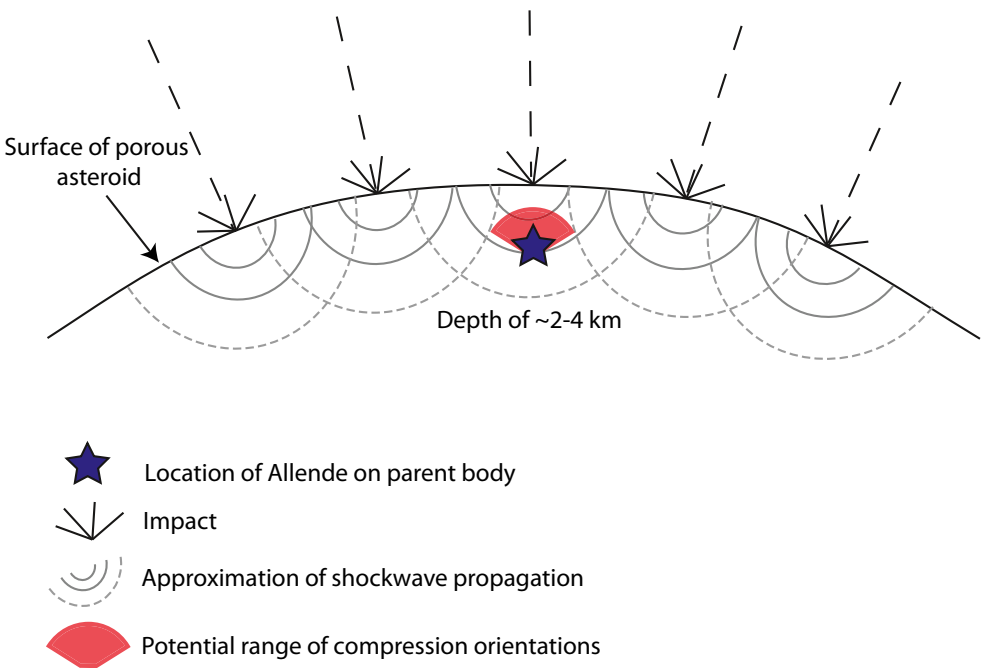

FIGURE 9. Simplified schematic of CV parent body, relative depth of Allende, and the orientations from which potential impacts may have affected the sample. The depth is based on findings related to the CV Kaba by Dodds et al. (2021) owing to a lack of depth estimation for Allende in the literature. (Color figure can be viewed at wileyonlinelibrary.com.)

parent body continued to form. Given how frequently impacts are predicted to have occurred in the early stages of solar system evolution (Ciesla et al., 2013), both during and after accretion, multiple, gentle impacts on the CV parent body are the most probable theory for creating the observations we see here. The multiple gentle impact theory is also supported by findings from experimental compaction research on the CV chondrites (Nakamura et al., 2000) and observations of flattened meso-scale features within unshocked CM chondrites (Lindgren et al., 2015).

CONCLUSIONS

We examined the CV3 chondrite Allende to assess geological evidence of impact-induced compaction at the meso- and micro-scales. Using high-resolution photography and EBSD analyses across multiple scales, we were able to build an integrated understanding of compaction across the different length scales and assess the likelihood of potential impact scenarios.

Meso-scale evidence of compression was observed as flattened and aligned CAIs across the 25 cm diameter slab (Figure 1) and chondrules and CAIs across the thin section WAM 13102. These components indicate an E–W compression occurred with respect to the frame of the sample in Figures 2 and 8. Micro-scale observations were made from multiple sources; high-resolution sites around chondrules and a CAI, and LAMs, firstly collected across an elongate CAI and secondly via reanalysis of LAM data from Forman et al. (2017) over a region of matrix and meso-scale components. Variations in CPO strength and orientation imply that these matrix zones record uniaxial compression in the general E–W, NNW–SSE, NW–SE, and NE–SW orientations.

The difference in apparent orientation of compression at the different scales here is attributed to Allende recording evidence of multiple, gentle impact events; meso-scale components are predicted to have flattened while matrix porosity was very high; however, the matrix may record evidence of subsequent impact events as porosity is highly likely to have remained after the first compactional impact based on experimental findings (Nakamura et al., 1995, 2000). We therefore predict at least one impact occurred in the E–W orientation in the plane of this sample (Figure 8) to flatten the meso-scale components, followed by multiple, gentle impacts in the NW–SE and NE–SW orientations to generate weak–moderate CPOs in the matrix regions. A simplified schematic indicated this ~125° variation in impact orientation is not only possible, but likely, while Allende resided on the CV parent body. This theory of multiple impacts is supported by findings from the CM chondrite Murchison (Lindgren et al., 2015), and also experimental findings from the CV chondrites (Nakamura et al., 2000).

The CAI examined here was a fine-grained type and presented an internal lineation petrofabric unlike the planar flattening textures seen elsewhere in the sample. We conclude that this is evidence of "flow" of a CAI in response to shockwave attenuation, as predicted by Tait et al. (2016), whereby highly malleable and porous CAIs fill their own porosity first at initial compression events, and then "flow" into nearby pores in response to further impacts. This is the first crystallographic evidence of this kind found in Allende and is supported by meso-scale findings of strain partitioning (Tait et al., 2016).

The integrated use of high-resolution photography, and both large area and high-resolution BSE and EBSD mapping enabled a development in our understanding of the effects of impact-induced compaction, directly comparable at different scales. The primary conclusion of this study—that Allende experienced multiple, gentle impacts on the parent body—may not have been arrived at if meso- and micro-scale impact evidence were explored in isolation. The collective geological histories of chondritic materials are complex, but with improved technology and integrated approaches such as that described here, we can further constrain the processes acting during asteroid formation and evolution within our solar system.

Acknowledgments—The authors thank the handling editor, Yves Marrocchi, and two reviewers, M. Zolensky and one anonymous reviewer, for their positive and supportive comments and suggestions, and for their time in considering this study. The authors thank C. Anders and G. Polley at the National Museum of Natural History for the contribution of Allende slab photographic images to this study. The authors wish to acknowledge the use of facilities and technical assistance at the John de Laeter Centre, Curtin University, and the use of raw data collected by Forman et al. (2017). LD would like to acknowledge funding from the University of Glasgow Early Career Mobility Scheme 2019 and funding from the UK Science Technology Facilities Council (STFC) grant (ST/T002328/1). Open access publishing facilitated by Curtin University, as part of the Wiley - Curtin University agreement via the Council of Australian University Librarians.

Data Availability Statement—Data available on request from the authors.

Editorial Handling—Dr. Yves Marrocchi

REFERENCES

Agnor, C., and Asphaug, E. 2004. Accretion Efficiency during Planetary Collisions. *The Astrophysical Journal* 613: L157–60. https://doi.org/10.1086/425158.

Bestmann, M., and Prior, D. J. 2003. Intragranular Dynamic Recrystallization in Naturally Deformed Calcite Marble: Diffusion Accommodated Grain Boundary Sliding as a Result of Subgrain Rotation Recrystallization. *Journal of Structural Geology* 25: 1597–613. https://doi.org/10.1016/s0191-8141(03)00006-3.

Bhattacharyya, D. S. 1966. Orientation of Mineral Lineation along the Flow Direction in Rocks. *Tectonophysics* 3: 29–33. https://doi.org/10.1016/0040-1951(66)90023-0.

Bland, P. A., Collins, G. S., Davison, T. M., Abreu, N. M., Ciesla, F. J., Muxworthy, A. R., and Moore, J. 2014. Pressure–Temperature Evolution of Primordial Solar System Solids during Impact-Induced Compaction. *Nature Communications* 5: 5451. https://doi.org/10.1038/ncomms6451.

Bland, P. A., Howard, L. E., Prior, D. J., Wheeler, J., Hough, R. M., and Dyl, K. A. 2011. Earliest Rock Fabric Formed in the Solar System Preserved in a Chondrule Rim. *Nature Geoscience* 4: 244–7. https://doi.org/10.1038/ngeo1120.

Bland, P. A., Jackson, M. D., Coker, R. F., Cohen, B. A., Webber, J. B. W., Lee, M. R., Duffy, C. M., et al. 2009. Why Aqueous Alteration in Asteroids Was Isochemical: High Porosity≠High Permeability. *Earth and Planetary Science Letters* 287: 559–68. https://doi.org/10.1016/j.epsl.2009.09.004.

Blum, J. 2003. The Structure of Planetesimals in the Solar Nebula. *Meteoritics & Planetary Science Supplement* 38: 5152.

Blum, J., and Schräpler, R. 2004. Structure and Mechanical Properties of High-Porosity Macroscopic Agglomerates Formed by Random Ballistic Deposition. *Physical Review Letters* 93: 115503. https://doi.org/10.1103/physrevlett.93.115503.

Bonal, L., Quirico, E., Bourot-Denise, M., and Montagnac, G. 2006. Determination of the Petrologic Type of CV3 Chondrites by Raman Spectroscopy of Included Organic Matter. *Geochimica et Cosmochimica Acta* 70: 1849–63. https://doi.org/10.1016/j.gca.2005.12.004.

Cain, P. M., McSween, H. Y., and Woodward, N. B. 1986. Structural Deformation of the Leoville Chondrite. *Earth and Planetary Science Letters* 77: 165–75. https://doi.org/10.1016/0012-821x(86)90158-5.

Ciesla, F. J., Davison, T. M., Collins, G. S., and O'Brien, D. P. 2013. Thermal Consequences of Impacts in the Early Solar System. *Meteoritics & Planetary Science* 48: 2559–76. https://doi.org/10.1111/maps.12236.

Corrigan, C. M., Zolensky, M. E., Dahl, J., Long, M., Weir, J., Sapp, C., and Burkett, P. J. 1997. The Porosity and Permeability of Chondritic Meteorites and Interplanetary Dust Particles. *Meteoritics & Planetary Science* 32: 509–15. https://doi.org/10.1111/j.1945-5100.1997.tb01296.x.

Daly, L., Piazolo, S., Lee, M. R., Griffin, S., Chung, P., Campanale, F., Cohen, B. E., et al. 2019. Understanding the Emplacement of Martian Volcanic Rocks Using Petrofabrics of the Nakhlite Meteorites. *Earth and Planetary Science Letters* 520: 220–30. https://doi.org/10.1016/j.epsl.2019.05.050.

Davison, T. M., Ciesla, F. J., and Collins, G. S. 2012. Post-Impact Thermal Evolution of Porous Planetesimals. *Geochimica et Cosmochimica Acta* 95: 252–69. https://doi.org/10.1016/j.gca.2012.08.001.

Davison, T. M., Collins, G. S., and Bland, P. A. 2014. Mesoscale Numerical Modeling of Compaction of Primitive Solar System Solids in Low-Velocity Collisions. 45th Lunar and Planetary Science Conference, p. 2718.

Davison, T. M., Collins, G. S., and Bland, P. A. 2016. Mesoscale Modeling of Impact Compaction of Primitive Solar System Solids. *The Astrophysical Journal* 821: 68. https://doi.org/10.3847/0004-637x/821/1/68.

Davison, T. M., Derrick, J. G., Collins, G. S., Bland, P. A., Rutherford, M. E., Chapman, D. J., and Eakins, D. E. 2017. Impact-Induced Compaction of Primitive Solar System Solids: The Need for Mesoscale Modelling and Experiments. *Procedia Engineering* 204: 405–12. https://doi.org/10.1016/j.proeng.2017.09.801.

Dodd, R. T. 1981. Meteorites, a Petrologic-Chemical Synthesis. CUP Archive, 368.

Dodds, K. H., Bryson, J. F. J., Neufeld, J. A., and Harrison, R. J. 2021. The Structure and Accretionary History of the CVox Parent Body Constrained from the Magnetization of Kaba. 52nd Lunar and Planetary Science Conference. LPI Contribution no. 2548, p. 2133.

Forman, L. V., Bland, P. A., Timms, N. E., Collins, G. S., Davison, T. M., Ciesla, F. J., Benedix, G. K., et al. 2016. Hidden Secrets of Deformation: Impact-Induced Compaction within a CV Chondrite. *Earth and Planetary Science Letters* 452: 133–45. https://doi.org/10.1016/j.epsl.2016.07.050.

Forman, L. V., Bland, P. A., Timms, N. E., Daly, L., Benedix, G. K., Trimby, P. W., Collins, G. S., and Davison, T. M. 2017. Defining the Mechanism for Compaction of the CV Chondrite Parent Body. *Geology* 45: 559–62. https://doi.org/10.1130/g38864.1.

Forman, L. V., Timms, N. E., Bland, P. A., Daly, L., Benedix, G. K., and Trimby, P. W. 2019. A Morphologic and Crystallographic Comparison of CV Chondrite Matrices. *Meteoritics & Planetary Science* 54: 2633–51. https://doi.org/10.1111/maps.13380.

Fritz, J., Greshake, A., and Fernandes, V. A. 2017. Revising the Shock Classification of Meteorites. *Meteoritics & Planetary Science* 52: 1216–32. https://doi.org/10.1111/maps.12845.

Gail, H.-P., Henke, S., and Trieloff, M. 2015. Thermal Evolution and Sintering of Chondritic Planetesimals—II. Improved Treatment of the Compaction Process. *Astronomy & Astrophysics* 576: A60. https://doi.org/10.1051/0004-6361/201424278.

Grimm, R. E., and Mcsween, H. Y. 1989. Water and the Thermal Evolution of Carbonaceous Chondrite Parent Bodies. *Icarus* 82: 244–80. https://doi.org/10.1016/0019-1035(89)90038-9.

Hanna, R. D., Ketcham, R. A., Zolensky, M., and Behr, W. M. 2015. Impact-Induced Brittle Deformation, Porosity Loss, and Aqueous Alteration in the Murchison CM Chondrite. *Geochimica et Cosmochimica Acta* 171: 256–82. https://doi.org/10.1016/j.gca.2015.09.005.

Henke, S., Gail, H. P., Trieloff, M., Schwarz, W. H., and Kleine, T. 2012. Thermal Evolution and Sintering of Chondritic Planetesimals. *Astronomy & Astrophysics* 537: A45. https://doi.org/10.1051/0004-6361/201117177.

Keil, K. 2000. Thermal Alteration of Asteroids: Evidence from Meteorites. *Planetary and Space Science* 48: 887–903. https://doi.org/10.1016/s0032-0633(00)00054-4.

Keller, L. P., Thomas, K. L., Clayton, R. N., Mayeda, T. K., DeHart, J. M., and McKay, D. S. 1994. Aqueous

Alteration of the Bali CV3 Chondrite: Evidence from Mineralogy, Mineral Chemistry, and Oxygen Isotopic Compositions. *Geochimica et Cosmochimica Acta* 58: 5589–98. https://doi.org/10.1016/0016-7037(94)90252-6.

Kimura, M., Grossman, J. N., and Weisberg, M. K. 2008. Fe-Ni Metal in Primitive Chondrites: Indicators of Classification and Metamorphic Conditions for Ordinary and CO Chondrites. *Meteoritics & Planetary Science* 43: 1161–77. https://doi.org/10.1111/j.1945-5100.2008.tb01120.x.

Lezzi, G., and Ventura, G. 2002. Crystal Fabric Evolution in Lava Flows: Results from Numerical Simulations. *Earth and Planetary Science Letters* 200: 33–46. https://doi.org/10.1016/s0012-821x(02)00617-9.

Lindgren, P., Hanna, R. D., Dobson, K. J., Tomkinson, T., and Lee, M. R. 2015. The Paradox Between Low Shock-Stage and Evidence for Compaction in CM Carbonaceous Chondrites Explained by Multiple Low-Intensity Impacts. *Geochimica et Cosmochimica Acta* 148: 159–78. https://doi.org/10.1016/j.gca.2014.09.014.

Lorenz, C., Ivanova, M., Krot, A., and Shuvalov, V. 2019. Formation of Disk- and Bowl-Shaped Igneous Ca,Al-Rich Inclusions: Constraints from Their Morphology, Textures, Mineralogy and Modelling. *Geochemistry* 79: 125523. https://doi.org/10.1016/j.chemer.2019.07.005.

Macke, R. J., Consolmagno, G. J., and Britt, D. T. 2011. Density, Porosity, and Magnetic Susceptibility of Carbonaceous Chondrites. *Meteoritics & Planetary Science* 46: 1842–62. https://doi.org/10.1111/j.1945-5100.2011.01298.x.

MacPherson, G. J. 2014. Treatise on Geochemistry. pp. 139–79. https://doi.org/10.1016/b978-0-08-095975-7.00105-4.

McCoy, T. J. 2010. Mineralogical Evolution of Meteorites. *Elements* 6: 19–23. https://doi.org/10.2113/gselements.6.1.19.

Merle, O. 1998. Internal Strain within Lava Flows from Analogue Modelling. *Journal of Volcanology and Geothermal Research* 81: 189–206. https://doi.org/10.1016/s0377-0273(98)00009-2.

Muxworthy, A. R., Bland, P. A., Davison, T. M., Moore, J., Collins, G. S., and Ciesla, F. J. 2017. Evidence for an Impact-Induced Magnetic Fabric in Allende, and Exogenous Alternatives to the Core Dynamo Theory for Allende Magnetization. *Meteoritics & Planetary Science* 52: 2132–46. https://doi.org/10.1111/maps.12918.

Nakamura, T., Tomeoka, K., Sekine, T., and Takeda, H. 1995. Impact-Induced Chondrule Flattening in the Allende CV3 Carbonaceous Chondrite: Shock Experiments. *Meteoritics* 30: 344–7. https://doi.org/10.1111/j.1945-5100.1995.tb01133.x.

Nakamura, T., Tomeoka, K., Takaoka, N., Sekine, T., and Takeda, H. 2000. Impact-Induced Textural Changes of CV Carbonaceous Chondrites: Experimental Reproduction. *Icarus* 146: 289–300. https://doi.org/10.1006/icar.2000.6385.

Nakamura, T., Tomeoka, K., and Takeda, H. 1992. Shock Effects of the Leoville CV Carbonaceous Chondrite: A Transmission Electron Microscope Study. *Earth and Planetary Science Letters* 114: 159–70. https://doi.org/10.1016/0012-821x(92)90158-r.

Ormel, C. W., Cuzzi, J. N., and Tielens, A. G. G. M. 2008. Co-Accretion of Chondrules and Dust in the Solar Nebula. *The Astrophysical Journal* 679: 1588–610. https://doi.org/10.1086/587836.

Rubin, A. E., and Swindle, T. D. 2011. Flattened Chondrules in the LAP 04581 LL5 Chondrite: Evidence for an Oblique Impact into LL3 Material and Subsequent Collisional Heating. *Meteoritics & Planetary Science* 46: 587–600. https://doi.org/10.1111/j.1945-5100.2011.01176.x.

Schmus, W. R. V., and Wood, J. A. 1967. A Chemical-Petrologic Classification for the Chondritic Meteorites. *Geochimica et Cosmochimica Acta* 31: 747–65. https://doi.org/10.1016/s0016-7037(67)80030-9.

Scott, E. R. D., Keil, K., and Stöffler, D. 1992. Shock Metamorphism of Carbonaceous Chondrites. *Geochimica et Cosmochimica Acta* 56: 4281–93. https://doi.org/10.1016/0016-7037(92)90268-n.

Sears, D., and Dodd, R. T. 1988. Overview and Classification of Meteorites. In *Meteorites and the Early Solar System*, edited by J. F. Kerridge and M. S. Matthews, 3–31. Tuscon: University of Arizona Press.

Sharp, T. G., and DeCarli, P. S. 2006. Shock Effects in Meteorites. In *Meteorites and the Early Solar System II*, edited by D. S. Lauretta and H. Y. McSween, 653–77. Tuscon: University of Arizona Press.

Stöffler, D., Keil, K., and Scott, E. R. D. 1991. Shock Metamorphism of Ordinary Chondrites. *Geochimica et Cosmochimica Acta* 55: 3845–67. https://doi.org/10.1016/0016-7037(91)90078-j.

Tait, A. W., Fisher, K. R., Srinivasan, P., and Simon, J. I. 2016. Evidence for Impact Induced Pressure Gradients on the Allende CV3 Parent Body: Consequences for Fluid and Volatile Transport. *Earth and Planetary Science Letters* 454: 213–24. https://doi.org/10.1016/j.epsl.2016.09.015.

Tomeoka, K., Yamahana, Y., and Sekine, T. 1999. Experimental Shock Metamorphism of the Murchison CM Carbonaceous Chondrite. *Geochimica et Cosmochimica Acta* 63: 3683–703. https://doi.org/10.1016/s0016-7037(99)00149-0.

Ushikubo, T., Kimura, M., Kita, N. T., and Valley, J. W. 2012. Primordial Oxygen Isotope Reservoirs of the Solar Nebula Recorded in Chondrules in Acfer 094 Carbonaceous Chondrite. *Geochimica et Cosmochimica Acta* 90: 242–64. https://doi.org/10.1016/j.gca.2012.05.010.

Vacher, L. G., Marrocchi, Y., Villeneuve, J., Verdier-Paoletti, M. J., and Gounelle, M. 2018. Collisional and Alteration History of the CM Parent Body. *Geochimica et Cosmochimica Acta* 239: 213–34. https://doi.org/10.1016/j.gca.2018.08.006.

Watt, L. E., Bland, P. A., Prior, D. J., and Russell, S. S. 2006. Fabric Analysis of Allende Matrix Using EBSD. *Meteoritics & Planetary Science* 41: 989–1001.

Weidenschilling, S. J. 2019. Accretion of the Asteroids: Implications for their Thermal Evolution. *Meteoritics & Planetary Science* 54: 1115–32. https://doi.org/10.1111/maps.13270.

Weidenschilling, S. J., and Cuzzi, J. N. 2006. Accretion Dynamics and Timescales: Relation to Chondrites. In *Meteorites and the Early Solar System II*, edited by D. S. Lauretta and H. Y. McSween, 473–85. Tuscon: University of Arizona Press